



# Bi<sub>2</sub>MoO<sub>6</sub> co-modified by reduced graphene oxide and palladium (Pd<sup>2+</sup> and Pd<sup>0</sup>) with enhanced photocatalytic decomposition of phenol



Xiangchao Meng, Zisheng Zhang\*

Department of Chemical and Biological Engineering, University of Ottawa, Ottawa, Ontario K1N 6N5, Canada

## ARTICLE INFO

### Article history:

Received 10 September 2016

Received in revised form 7 January 2017

Accepted 12 January 2017

Available online 17 January 2017

### Keywords:

Photocatalysis

Graphene

SPR

Bi<sub>2</sub>MoO<sub>6</sub>

Palladium

## ABSTRACT

A ternary Bi<sub>2</sub>MoO<sub>6</sub> photocatalyst composite was hybridized for the first time, with reduced graphene oxide (rGO) and palladium (Pd) nanoparticles decorated on the surface. As-prepared composites exhibited excellent photocatalytic activity in the degradation of organic pollutants (phenol) in wastewater under visible light irradiation. The enhanced photocatalytic performance when rGO and Pd nanoparticles combined with Bi<sub>2</sub>MoO<sub>6</sub> may be attributed to the reduction of the recombination rate of photogenerated electrons/holes. Specifically, the rGO layer may serve as the electron accepter, which means photogenerated electrons can rapidly transfer to its surface instead of jumping back to the valence band and combining with positive holes. Additionally, the black-body property of graphite-like material contribute the increased harvesting capacity of visible-light photons. Furthermore, palladium nanoparticles distributed on the surface can also be stimulated by visible light photons due to the surface plasmon resonance effect, which further increased the utilization efficiency of visible light irradiation. This work opens a new possibility for efficient removal of phenolic compounds in wastewater via visible light-driven photocatalysis in the presence of a Pd-rGO- Bi<sub>2</sub>MoO<sub>6</sub> ternary composite.

© 2017 Elsevier B.V. All rights reserved.

## 1. Introduction

Bismuth-based visible light-driven photocatalysts have attracted extensive interests of researchers, and have exhibited strong potential for industrialization from an economic stand-point compared to the most widely studied UV-driven photocatalysts, such as TiO<sub>2</sub> [1–4]. Two main application areas of photocatalysis can be summarized as water-splitting to generate H<sub>2</sub> and degradation of organic pollutants in wastewater [5,6]. When choosing a semiconductor for water splitting to generate both H<sub>2</sub> and O<sub>2</sub>, two crucial factors must be considered: the availability of electrons on the conduction band for stronger capacity to reduce H<sup>+</sup> to H<sub>2</sub>, and the maximum potential of a valence band being higher than the redox potential of O<sub>2</sub>/H<sub>2</sub>O. For bismuth-based photocatalyst semiconductors, the conduction bands are rarely suitable for the production of H<sub>2</sub> without modulation of the energy band as reported in [4]. Instead, photogenerated holes on the valence bands of bismuth-based semiconductors are usually oxidative enough to decompose most of the organic pollutants in wastewater.

Bi<sub>2</sub>MoO<sub>6</sub>, as a member of Aurivillius family, was originally considered because of their ferroelectric properties [7]. Recent results revealed that Bi<sub>2</sub>MoO<sub>6</sub> may be a potential candidate as a visible light-driven photocatalyst applied in oxidizing organics in wastewater [8]. However, the relatively high recombination rate of photogenerated electrons/holes pairs for pure Bi<sub>2</sub>MoO<sub>6</sub>, when illuminated under visible light irradiation, hinders its widely application. Approaches such as doping [9,10] and heterojunction formation [11] have been adopted to suppress the recombination of photo-generated e<sup>-</sup>/h<sup>+</sup> pairs. Among them, reduced graphene oxide (rGO) integrated Bi<sub>2</sub>MoO<sub>6</sub> hybrid photocatalysts were reported with enhanced photocatalytic activity and opened new possibilities in environmental remediation using solar energy [12–15]. Graphene, which is a single layer of sp<sup>2</sup>-bonded carbon atoms tightly packed into a two-dimensional honeycomb structure, has been extensively studied due to its excellent physiochemical properties [16]. It is proven to be an effective and inexpensive way to produce graphene nanosheets by reducing graphene oxide (GO). Graphene is regarded as an excellent electrons accepter. As a result, electrons photogenerated by Bi<sub>2</sub>MoO<sub>6</sub> activated by light irradiation may be easily transferred to the wide graphene layer, so as to reduce their recombination rate and improve the photocatalytic activity. It was reported that silver nanoparticles decorated on the surface of Bi<sub>2</sub>MoO<sub>6</sub> can greatly improve its performance in photocatalysis [17].

\* Corresponding author.

E-mail addresses: [xmeng086@uottawa.ca](mailto:xmeng086@uottawa.ca) (X. Meng), [\(Z. Zhang\)](mailto:zhang@uottawa.ca).

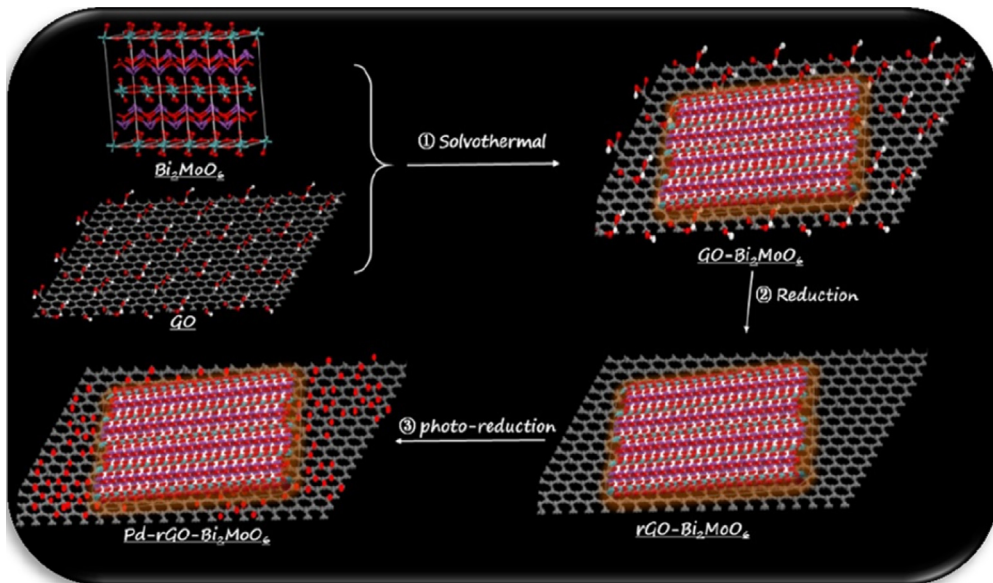


**Fig. 1.** Scheme of preparation processes of Pd-rGO-Bi<sub>2</sub>MoO<sub>6</sub>.

sis, which can also be activated by visible light photons via surface plasmon resonance (SPR) effect [10,17]. The SPR peaks of Palladium nanoparticles, as reported, can be tuned from 410 nm to 870 nm [18,19]. Also, 2D rGO sheets decorated with palladium nanoparticles were reported for efficient degradation of organic dyes [20,21]. We recently have prepared Pd nanoparticle decorated Bi<sub>2</sub>MoO<sub>6</sub> hybrid photocatalysts, Pd-Bi<sub>2</sub>MoO<sub>6</sub>, and they exhibited enhanced visible-light-driven photocatalytic activity in the degradation of organic pollutants in wastewater [22]. Compared with the chemical deposition method to doping metal ions [23–25], the photoreduction approach to load metallic nanoparticles on the surface is more facile. Moreover, metallic nanoparticles promote the effective separation of the photogenerated charge carriers and also improve the visible light-responsivity because of the SPR effect. It is reported the metallic nanoparticles are more stable when they present in the forms of both metallic and ionic valence states [26], suggesting the structure of Pd<sup>0</sup>/Pd<sup>2+</sup> is supposed to be more stable compared to bare Pd<sup>0</sup>. Recently, Bi et al. have reported on the preparation of ternary Au-rGO-Bi<sub>2</sub>MoO<sub>6</sub> composites with enhanced photocatalytic activities under visible light irradiation [27]. Based on above reported work, a ternary (metallic nanoparticles)-rGO-Bi<sub>2</sub>MoO<sub>6</sub> composite is supposed to be a promising photocatalyst and need to be further developed [28]. Palladium may be one of the promising candidates, owing for its electrophilicity for facilitating the uptake of photogenerated electrons [29].

This work reports the preparation of a ternary composite composed of Pd, rGO and Bi<sub>2</sub>MoO<sub>6</sub>. The visible light-driven photocatalytic activities of prepared samples were measured by degrading a colorless organic model, phenol which is widely found in wastewater from many industrial processes and generally difficult to decompose by traditional methods due to its high chemical stability [30,31]. This work has shed light on the possibility of using photocatalysis for treating phenolic compounds in wastewater under visible light irradiation.

## 2. Experimental

### 2.1. Preparation of rGO-Bi<sub>2</sub>MoO<sub>6</sub>

The GO-Bi<sub>2</sub>MoO<sub>6</sub> composites were first prepared by the one-pot solvothermal method, as shown in Fig. 1. In a typical process,

264 μL of graphene oxide (GO, dissolved in H<sub>2</sub>O with concentration of 4 mg/mL, Sigma-Aldrich Canada) were dissolved in 20 mL ethanol and the suspension was sonicated for 1 h. Next, 1.68 g of Bi(NO<sub>3</sub>)<sub>3</sub>·5H<sub>2</sub>O (Fisher Scientific Canada, Certified ACS) was dissolved in 5 mL of ethylene glycol (EG, analytical purity, Fisher Scientific Canada) and 0.42 g of Na<sub>2</sub>MoO<sub>4</sub>·2H<sub>2</sub>O (Fisher Scientific Canada, Certified ACS) was also dissolved in another 5 mL of EG. These three mixtures were then mixed together via magnetic stirring for 30 min. The mixture was then transferred to a 45-mL Teflon-lined stainless steel autoclave (Parr Instrument Company, USA) and heated at 160 °C for 20 h. The autoclave was then allowed to naturally cool down to room temperature. The precipitates were then filtered out and washed once with ethanol and twice with distilled deionized water (DD Water). The washed samples were then dried at 60 °C overnight before being collected. As-prepared GO-Bi<sub>2</sub>MoO<sub>6</sub> composites were further reduced as reported in [32]. Typically, 0.50 g of GO-Bi<sub>2</sub>MoO<sub>6</sub> composites were added in 50 mL EG and ultrasonicated for 30 min. The mixture was then heated and stirred at 140 °C for 2 h. The particle sample was then separated out, washed by ethanol and dried at 60 °C overnight before being collected. For comparison, pure Bi<sub>2</sub>MoO<sub>6</sub> was also prepared using the solvothermal method without adding GO in the precursor solution.

### 2.2. Preparation of Pd-rGO-Bi<sub>2</sub>MoO<sub>6</sub>

Pd-rGO-Bi<sub>2</sub>MoO<sub>6</sub> composite samples were synthesized by a photoreduction method, as shown in Fig. 1. In a typical procedure, 0.30 g of as-prepared rGO-Bi<sub>2</sub>MoO<sub>6</sub> composites were suspended in 40 mL DD Water and sonicated for 30 min before adding a designated amount of PdCl<sub>2</sub> (Fisher Scientific Canada, ACS certified). The mixture was then magnetically stirred for 10 min, and illuminated under a 300-W halogen tungsten projector lamp (wavelength: 310–800 nm, Ushio, USA) for 1 h. After that, the resultant products were separated out via centrifugation, washed twice with DDW and dried at 60 °C overnight. Samples of 0.5, 1, 2 and 4 wt% Pd-rGO-Bi<sub>2</sub>MoO<sub>6</sub> were prepared following the above procedures. For comparison, 2 wt% Pd-Bi<sub>2</sub>MoO<sub>6</sub> were also prepared by changing the substrate to Bi<sub>2</sub>MoO<sub>6</sub> instead of rGO-Bi<sub>2</sub>MoO<sub>6</sub>. Also, 2 wt% Pd-rGO composites were prepared by using NaBH<sub>4</sub> (Fisher Scientific Canada, 98%) as the reducing agent [20].

### 2.3. Characterization

Crystal structures of prepared samples were investigated by X-ray diffraction (XRD) on a Rigaku Ultima IV Diffractometer with Cu K $\alpha$  radiation ( $\lambda = 0.15418$  nm) at 40 kV and 44 mA. XRD patterns were recorded at  $2\theta$  of 5–80°. Surface composition and chemical states of the samples were analyzed using a XSAM-800 X-ray Photoelectron Spectroscopy (XPS). The morphologies of prepared samples were investigated via scanning electron microscopy (SEM, model: JEOL JSM-7500F) equipped with energy dispersive X-ray spectroscopy (EDS) and transmission electron microscopy (TEM, model: JEM-2100F). The specific surface area, pore volume and average pore size were obtained from N<sub>2</sub> sorption isotherms at 77 K, using automatic adsorption apparatus and measurement systems (ASAP 2020, Micromeritics and Nova 4200E, Quantachrome). The Brunauer, Emmett and Teller (BET) surface area of the samples were calculated using multi-point estimation. The pore volumes were calculated using the volumes of adsorbed N<sub>2</sub> at  $p/p_0 = 0.977$ . Pore volume distributions are calculated using N<sub>2</sub> desorption branch, and the Barrett-Joyner-Halenda (BJH) method was used for the desorption branch to calculate the pore size data ( $d_p$ ) using Eq. (1) (where  $V/A_s$  is the ratio of volume to surface area of pores) as follows,

$$d_p = 4 \left( \frac{V}{A_s} \right)_{BJH} \quad (1)$$

A thermos Evolution 300 spectrophotometer was applied to measure the optical properties of samples through ultraviolet-visible diffuse reflectance spectra (DRS). Fourier Transform Infrared Spectroscopy (FTIR) was performed on a Cary 630 (Agilent Technologies). The spectra were recorded at room temperature with wavenumbers ranging from 2000 to 600 cm<sup>-1</sup>. Electrochemical properties of prepared samples were analyzed on a CHI 604E electrochemical analyzer (CH Instruments Inc., USA) with a platinum wire as a counter electrode, a calomel reference electrode and a working electrode. The working electrode composed of indium tin oxide (ITO, 75 × 25 × 1.1 mm, 15–25 Ω, Sigma-Aldrich Canada Co.), glass coated with the prepared samples. The electrochemical impedance spectroscopies (EIS) were recorded with frequencies in the range of 1–1,000,000 Hz and a sinusoidal wave of 5 mV. The electrolyte was Na<sub>2</sub>SO<sub>4</sub> with a concentration of 0.5 mol/L.

### 2.4. Photocatalytic activity tests

Photocatalytic activities of prepared samples were measured with regard to degrading the colorless organic pollutant model compound (phenol) under visible light irradiation. Specifically, a 500-mL beaker with a cooling jacket served as the reactor. The temperature of the reacting solution was kept at ~20 °C for all tests. The light source composed of a 300-W halogen tungsten projector lamp (Ushio, USA) with wavelengths mainly in the range of 310–800 nm. A cut-off (Kenko Zeta, transmittance >90%) was used to filter out wavelengths below 410 nm to ensure the irradiation occurred within visible light range. The irradiation intensity on the surface of the solution was measured on a quantum meter (Biospherical QSL-2100, 400 < λ < 700 nm) to be, on average,  $1.1 \times 10^{-2}$  Einsteins m<sup>-2</sup> s<sup>-1</sup>. In each test, 100 mL of phenol with a concentration of 10 ppm (mg/L) was mixed with 0.1 g (1.0 g<sub>cat</sub>/L<sub>solution</sub>) of as-prepared photocatalyst composites. This suspension was first magnetically stirred for 60 min in the dark before turning on the lamp, aiming to reach an adsorption-desorption equilibrium between the organic pollutants and the photocatalysts. The photocatalytic tests last for 6 h, and aliquots were drawn every 30 min. After centrifuging at 13,000 rpm for 5 min, the supernatant was analyzed using a high-performance liquid chromatograph (HPLC, Agilent 1100 series) equipped with a UV-vis detector. A ZORBAX

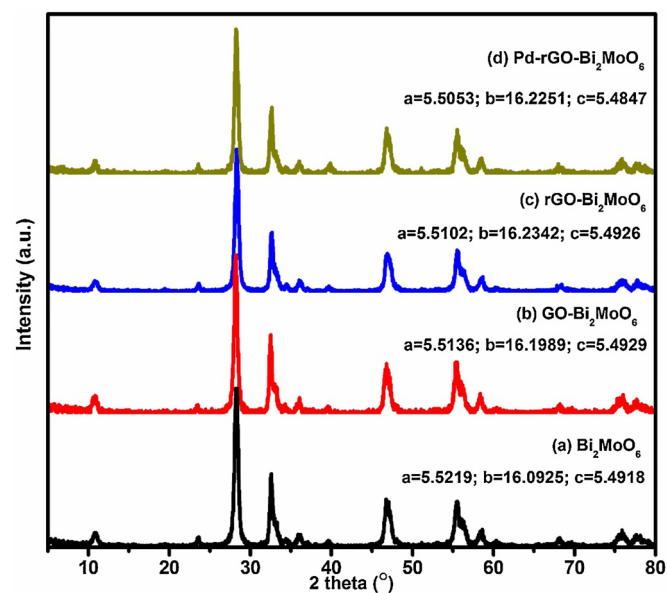


**Fig. 2.** XRD patterns of as-prepared composites: (a) pure Bi<sub>2</sub>MoO<sub>6</sub>, (b) GO-Bi<sub>2</sub>MoO<sub>6</sub>, (c) rGO-Bi<sub>2</sub>MoO<sub>6</sub> and (d) Pd-rGO-Bi<sub>2</sub>MoO<sub>6</sub>.

Eclipse Plus C18 column (4.6 × 250 mm) was used at a temperature of 60 °C. The detecting wavelength was fixed at 270 nm for the detection of phenol and possible intermediates. The flow phase was composed of methanol (55%, V/V) and water (45%, V/V) at a flow rate of 0.6 mL/min. The injection volume was set to 25 μL.

To measure the reusability of prepared photocatalysts, 2 wt% Pd-rGO-Bi<sub>2</sub>MoO<sub>6</sub> composites were recycled for four times in total. Photocatalysts were separated out from the suspension following a single run, and then mixed with fresh wastewater to start another run.

### 2.5. Electronic structure calculation

The quantum-mechanical calculations were performed on the basis of the density functional theory (DFT) [33]. The generalized gradient approximation (GGA) was applied to exchange-correlation effects. The open access software Quantum ESPRESSO was used, which utilizes pseudo potentials to describe electron-ion interactions and represents electronic wave functions using a plane-wave basis set [34]. The kinetic energy cut-off was set to 300 eV.

## 3. Results and discussions

### 3.1. XRD and XPS

The crystal structures of as-prepared pure Bi<sub>2</sub>MoO<sub>6</sub> and modified Bi<sub>2</sub>MoO<sub>6</sub> composites were studied by XRD, patterns of which were shown in Fig. 2. As for patterns of pure Bi<sub>2</sub>MoO<sub>6</sub>, all identifiable peaks agree well with an orthorhombic crystal structure (space group: pbca (61), PDF card number:00-72-1524) [35]. Impurity peaks were not found, indicating that a well-crystallized Bi<sub>2</sub>MoO<sub>6</sub> sample was prepared by the solvothermal method. Patterns of GO, rGO, and Pd-rGO-modified Bi<sub>2</sub>MoO<sub>6</sub> composites exhibit negligible differences with those of pure Bi<sub>2</sub>MoO<sub>6</sub>, most likely due to the small quantity of these dopants. Specifically, the loading quantity of (r)GO (0.1 wt%) and Pd (4 wt%) in the composites were too small to be detected by XRD. The lattice parameters of pure Bi<sub>2</sub>MoO<sub>6</sub> were refined and calculated as:  $a = 5.5219$  Å,  $b = 16.0925$  Å, and  $c = 5.4918$  Å. The lattice parameters of Bi<sub>2</sub>MoO<sub>6</sub> in the GO-, rGO- and Pd-rGO- Bi<sub>2</sub>MoO<sub>6</sub> composites were also calculated and shown

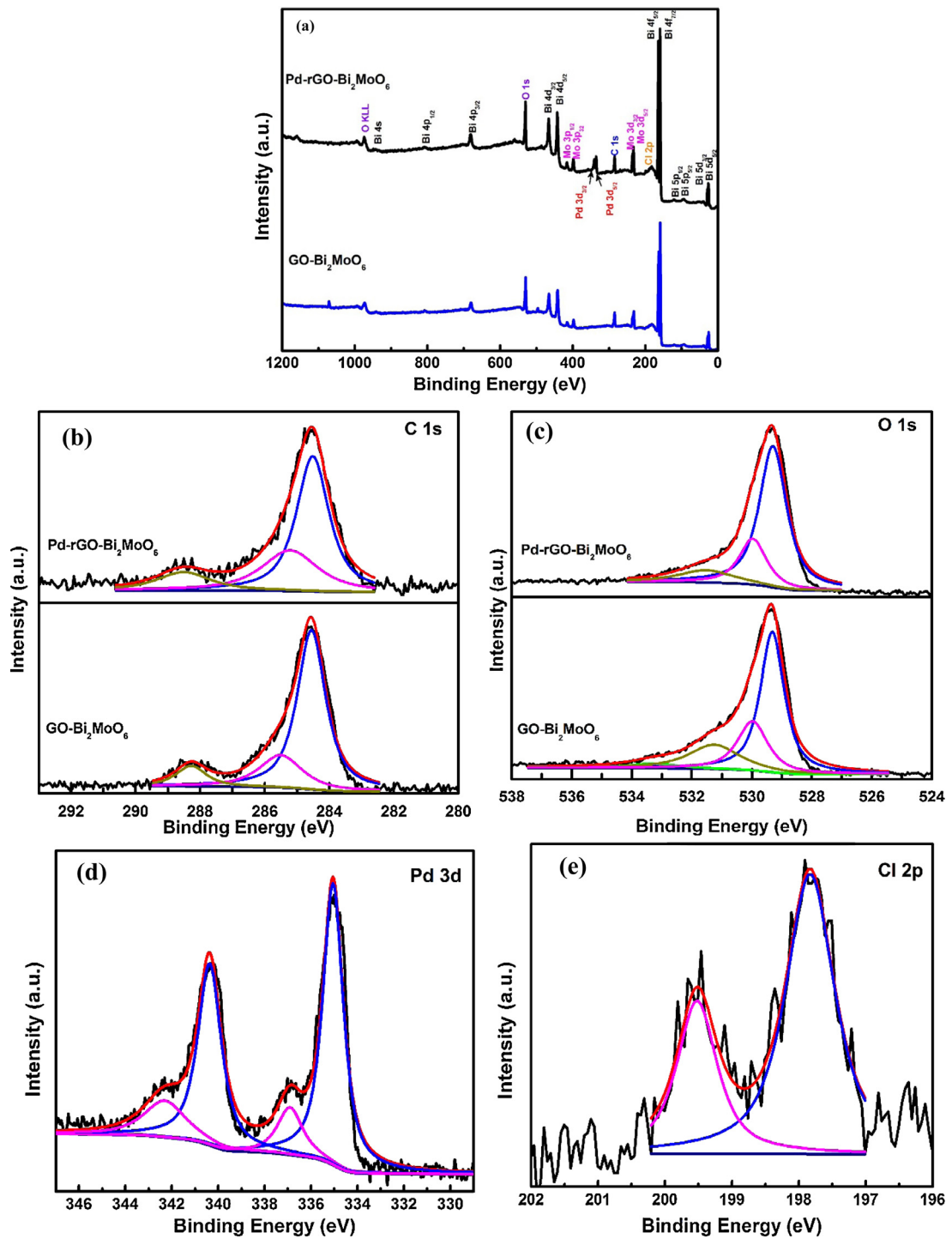


**Fig. 3.** (a) XPS survey spectra, and high –resolution orbits scan of (b) C 1s, (c) O 1s, (d) Pd 3d and (e) Cl 2p for GO- and Pd-rGO-Bi<sub>2</sub>MoO<sub>6</sub> composites, respectively.

in Fig. 2. It can be found that these dopants have negligible influence on Bi<sub>2</sub>MoO<sub>6</sub> crystal parameters.

To further explore the surface elements and chemical states of prepared composites, XPS survey spectra and high-resolution orbits scan for GO- and Pd-rGO-Bi<sub>2</sub>MoO<sub>6</sub> composites were depicted in Fig. 3. All spectra were calibrated with C 1s, the binding energy of which was fixed at 284.6 eV. In the survey spectra for GO-Bi<sub>2</sub>MoO<sub>6</sub> (Fig. 3a), all elements, namely C, O, Bi and Mo, were detected with strong characteristic peaks; no impurities were detected. When Pd were introduced in the composites, characteristic peaks for Pd were detected. For the C 1s orbits scan in Fig. 3b, three peaks located

at 284.6, 285.5 and 288.3 eV were found in the spectra for both GO- and Pd-rGO-Bi<sub>2</sub>MoO<sub>6</sub> composites, which can be attributed to the C–C, C–O, and O=C=O groups in the GO and rGO. The intensity of the peak for O=C=O was slightly reduced when the GO was reduced, indicating some of the oxygen functional groups were removed during the reduction process [36,37]. Furthermore, in the O 1s XPS spectra shown in Fig. 3c, four small peaks were detected for GO-Bi<sub>2</sub>MoO<sub>6</sub> composites, located at 529.8, 530.5, 531.3 and 533.2 eV, which may be attributed to Bi–O, Mo–O, C–O and C=O, respectively [38]. However, when GO was reduced, only three peaks were detected in the O 1s XPS spectrum for Pd-rGO-Bi<sub>2</sub>MoO<sub>6</sub>

composites. Here, the intensities of peaks for C—O and C=O were reduced, which suggests the oxygen functional groups were greatly removed by the reduction process. Meanwhile, two sets of spin-orbit doublets for Pd 3d were detected in the Pd-rGO-Bi<sub>2</sub>MoO<sub>6</sub> composites (Fig. 3d). Accordingly, Pd (3d<sub>3/2</sub>, 3d<sub>5/2</sub>) located at binding energies of 334.7 and 340.0 eV, as well as at 337.0 and 342.3 eV may be attributed to the metallic Pd<sup>0</sup> and Pd<sup>2+</sup>, respectively. The relative concentration of bivalent to metallic Pd can be calculated using Eq. (2) [39]:

$$\frac{\eta_{Pd^0}}{\eta_{Pd^{2+}}} = \frac{I_{Pd^0}}{I_{Pd^{2+}}} \times \frac{\sigma_{Pd} \lambda_{Pd} D_E(Pd)}{\sigma_{Pd} \lambda_{Pd} D_E(Pd)} = \frac{I_{Pd^0}}{I_{Pd^{2+}}} \quad (2)$$

where  $\eta$ ,  $I$ ,  $\sigma$ ,  $\lambda$ , and  $D_E$  are the surface concentration, integrated intensity, photoelectric cross-section, electron free mean path, and geometric factor, respectively. The values of  $\sigma$ ,  $\lambda$ , and  $D_E$  have been calculated and summarized by Penn and Scofield, and can be obtained from literature [40,41]. Integration areas of Pd<sup>0</sup> and Pd<sup>2+</sup> peaks were performed to estimate their concentrations. The relative combined surface concentration ratio of Pd<sup>0</sup> to Pd<sup>2+</sup> was approximately 3.7:1. Theoretically, the redox potential of Pd<sup>2+</sup>/Pd was 0.987 V. The bottom potential of the conduction band of Bi<sub>2</sub>MoO<sub>6</sub> can be calculated as 0.34 eV using Eq. (3):

$$E_{CB, Bi_2MoO_6} = X_{Bi_2MoO_6} - E^e - \frac{1}{2}E_g \quad (3)$$

where  $X_{Bi_2MoO_6}$  (6.13 eV),  $E^e$  and  $E_g$  are the electronegativity, the energy of free electrons on the hydrogen scale ( $\approx$ 4.5 eV), and the band gap of Bi<sub>2</sub>MoO<sub>6</sub> (2.58 eV, from Section 3.4) [42,43]. It means electrons on the conduction band of Bi<sub>2</sub>MoO<sub>6</sub> are reductive enough to reduce Pd<sup>2+</sup> to Pd. In addition, the high-resolution Cl 2p orbital scan shown in Fig. 3e further suggests the presence of PdCl<sub>2</sub> on the

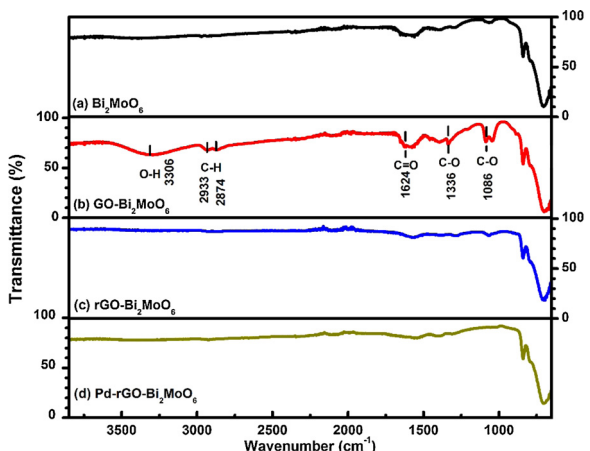


**Fig. 4.** FTIR spectra for (a) pure Bi<sub>2</sub>MoO<sub>6</sub> and (b) GO-, (c) rGO-, (d) Pd-rGO-Bi<sub>2</sub>MoO<sub>6</sub> composites.

surface of the Pd-Bi<sub>2</sub>MoO<sub>6</sub> composites. Peaks located at binding energies of 197.5 and 199.1 eV for Cl 2p<sub>1/2</sub> and Cl 2p<sub>3/2</sub>, respectively, clearly indicates the presence of Cl<sup>-</sup> [44]. It can be concluded that only a portion of Pd<sup>2+</sup> was reduced to metallic Pd in the photoreduction process.

### 3.2. FT-IR

FTIR spectra for as-prepared samples were shown in Fig. 4. For the spectrum of pure Bi<sub>2</sub>MoO<sub>6</sub>, the main absorbance bands at wavenumbers in the range of 1000–600 cm<sup>-1</sup> may be attributed

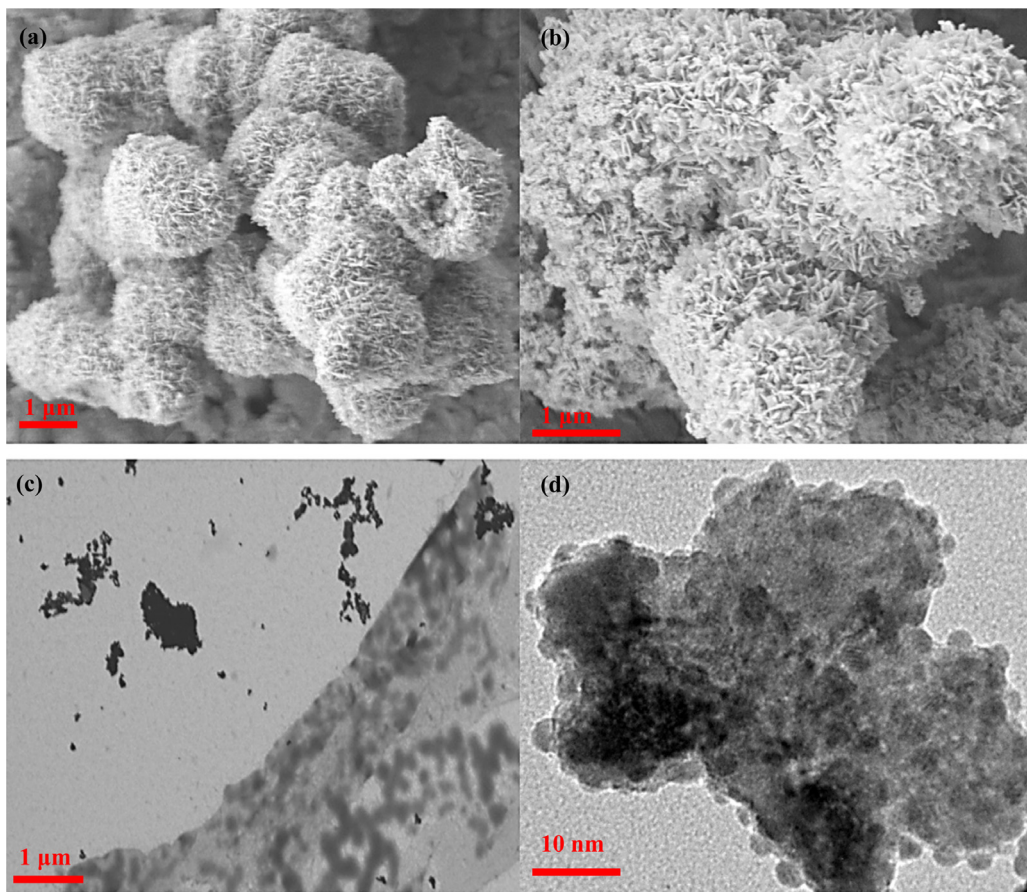


**Fig. 5.** SEM images for (a) pure Bi<sub>2</sub>MoO<sub>6</sub> and (b) Pd-rGO-Bi<sub>2</sub>MoO<sub>6</sub> composites, STEM image for Pd-rGO-Bi<sub>2</sub>MoO<sub>6</sub> composites, and TEM image for Pd-rGO-Bi<sub>2</sub>MoO<sub>6</sub> composites.

to Bi-O, Mo-O stretching and Mo-O bridging stretching modes [8]. The strongest absorbance peak at  $690\text{ cm}^{-1}$  may have resulted from the asymmetric stretching mode of  $\text{MoO}_6$  involving vibrations of the equatorial oxygen atoms. Two peaks at wavenumbers of 795 and  $845\text{ cm}^{-1}$  may be attributed to the asymmetric and symmetric stretching modes of  $\text{MoO}_6$  involving vibrations of the apical oxygen atoms [45,46]. When GO was added in the composites, small absorbance peaks at wavenumbers between  $3500$  and  $1000\text{ cm}^{-1}$  were found. Specifically, peaks at 3306, 2933, 2874, 2086, 1624, and  $1336\text{ cm}^{-1}$  can be related to  $-\text{OH}$ ,  $-\text{CH}_2-$ ,  $\text{C}-\text{O}$ ,  $\text{C}=\text{O}$ ,  $\text{C}-\text{O}-\text{C}$  (or H) stretching, respectively [47]. After the reduction process, it can be found that these absorbance peaks for these oxygen functional groups in the spectrum for rGO- $\text{Bi}_2\text{MoO}_6$  were weakened or removed. The  $\text{O}=\text{C}-\text{OH}$  may be completely reduced to C, as for the  $-\text{OH}$  peak disappears [32,48]. When Pd was loaded on the surface of rGO- $\text{Bi}_2\text{MoO}_6$ , the differences in the spectra were negligible.

### 3.3. Morphologies and possible formation processes

The morphologies of prepared pure  $\text{Bi}_2\text{MoO}_6$  and Pd-rGO- $\text{Bi}_2\text{MoO}_6$  were observed by SEM, STEM and TEM, and illustrated in Fig. 5. For pure  $\text{Bi}_2\text{MoO}_6$  in Fig. 5a, uniform hierarchical microspheres with a diameter of about  $2\text{ }\mu\text{m}$  were observed, and were composed of crystalline nanosheets. Hollow microspheres were also observed in Fig. 5a, which can be ascribed to the Ostwald ripening formation process [49,50]. When the reaction time is short, the  $\text{Bi}_2\text{MoO}_6$  sphere has a solid core. With a longer reaction time however, the dissolution-recrystallization process occurs, and crystalline nanosheets form on the outer surface by dissolving crystallites located in the inner cores. This may be due to crystallites at

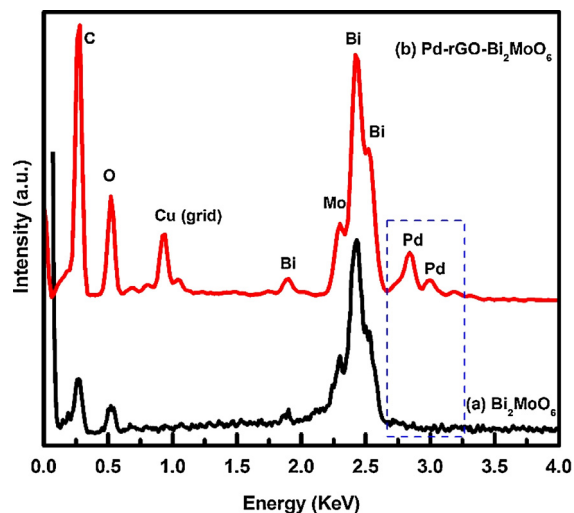


**Fig. 6.** EDS spectra for (a) pure  $\text{Bi}_2\text{MoO}_6$  and (b) Pd-rGO- $\text{Bi}_2\text{MoO}_6$  composites.

the inner core possessing higher surface energies than those at the outer surface. When the modifiers, namely Pd and rGO, were introduced on the surface of  $\text{Bi}_2\text{MoO}_6$ , flake-like particles were formed on the microspheres which can be seen from the SEM image in Fig. 5b. STEM was applied to explore the morphologies of GO; in Fig. 5c, the curly GO sheets were observed. In the high-resolution TEM image of Pd-rGO- $\text{Bi}_2\text{MoO}_6$  shown in Fig. 5d, nanoparticles with diameters of about 2–3 nm were observed. To confirm these nanoparticles are metallic palladium, EDS was applied and shown

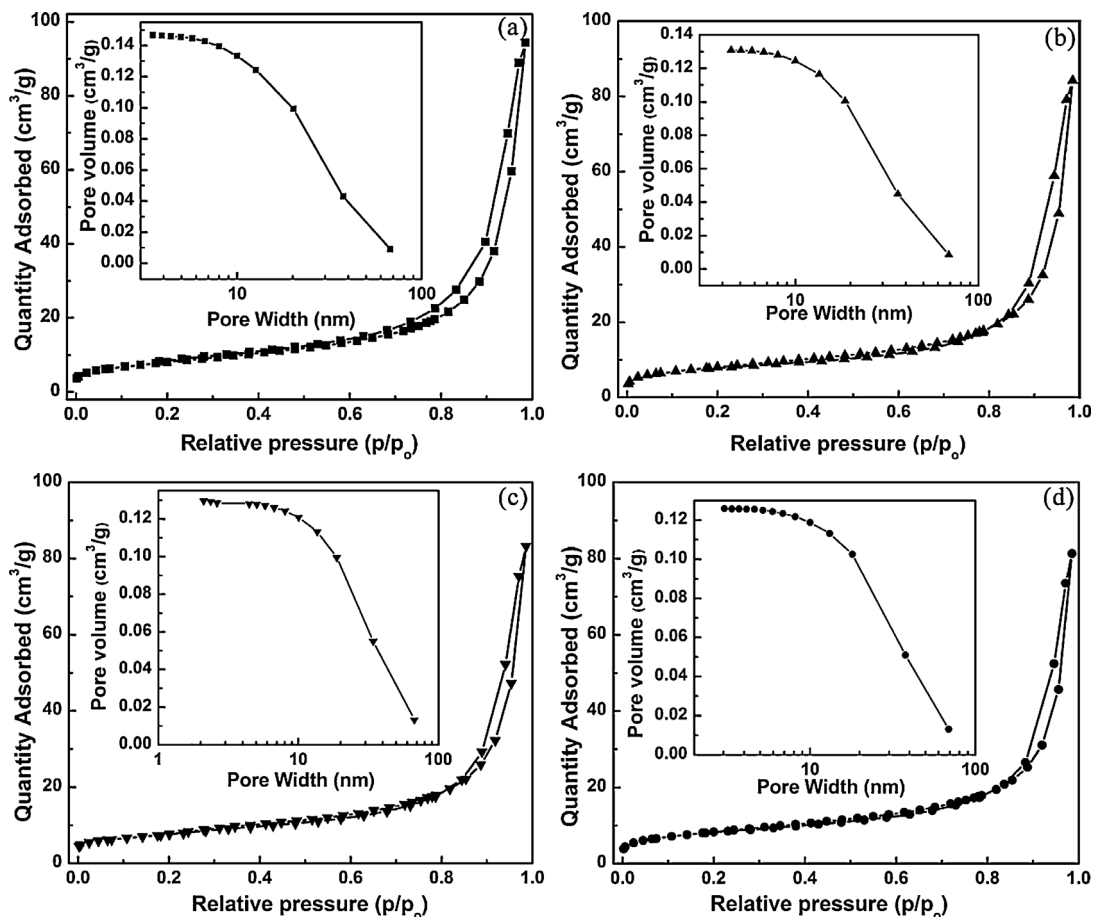


**Fig. 7.**  $\text{N}_2$  sorption isotherms and pore size distributions for (a)  $\text{Bi}_2\text{MoO}_6$ , (b) GO- $\text{Bi}_2\text{MoO}_6$ , (c) rGO- $\text{Bi}_2\text{MoO}_6$ , and (d) Pd-rGO- $\text{Bi}_2\text{MoO}_6$ , respectively.

**Table 1**

Specific surface area, pore volume, and average pore size of  $\text{Bi}_2\text{MoO}_6$ , GO- $\text{Bi}_2\text{MoO}_6$ , rGO- $\text{Bi}_2\text{MoO}_6$ , and Pd-rGO- $\text{Bi}_2\text{MoO}_6$  composites.

Sample	$S_{\text{BET}}$ ( $\text{m}^2/\text{g}$ )	Pore volume ( $\text{cm}^3/\text{g}$ )	Average pore size (nm)
$\text{Bi}_2\text{MoO}_6$	29	0.15	20.4
GO- $\text{Bi}_2\text{MoO}_6$	29	0.13	20.2
rGO- $\text{Bi}_2\text{MoO}_6$	30	0.13	18.8
Pd-rGO- $\text{Bi}_2\text{MoO}_6$	29	0.12	18.5

in Fig. 6. Peaks of Pd were found, which provided solid evidence that Pd nanoparticles were successfully formed on the surface. Meanwhile, the intensities of peaks for C and O in the EDS spectrum of Pd-rGO- $\text{Bi}_2\text{MoO}_6$  were greatly improved compared to those in the spectrum of  $\text{Bi}_2\text{MoO}_6$ . It also suggests GO was successfully combined in the composites.

### 3.4. $N_2$ sorption isotherms

Nitrogen sorption isotherms were obtained and shown in Fig. 7 for pure  $\text{Bi}_2\text{MoO}_6$ , GO- $\text{Bi}_2\text{MoO}_6$ , rGO- $\text{Bi}_2\text{MoO}_6$  and Pd-rGO- $\text{Bi}_2\text{MoO}_6$ . All isotherms are attributed to the combination of Type II and IV physisorption isotherms [51,52]. The type IV isotherm is typical for mesoporous material. An adsorbate monolayer is firstly formed under low pressures, followed by the multilayer adsorption under high pressures. However, the typical feature for type IV sorption isotherm, which is the final saturation plateau, is not observed for each isotherm in Fig. 7 [53]. This phenomenon may be caused by the shortage of capillary condensation in adsorption on the surface of macropores, which may have resulted in a rapid transition to type II isotherms. A hysteresis loop for each isotherm in Fig. 7 is observed, which is attributed to H3 type. The onset of the hysteresis loop indicates the beginning of the capillary condensation in the mesopores. At upper closure point, the mesopores are fully filled with liquid. The H3-type hysteresis loop may be attributed to the presence of aggregations of plate-like particles giving rise to slit-shaped pores, which agrees well with the morphologies observed in the SEM images [27,51]. Also, the pore size distributions for each sample are also plotted in the insets of Fig. 7. The mesopores may correspond to the pores formed by Ostwald ripening [49] and the voids between crystals within the two-dimensional layers and interspaces between these stacked layers. The specific surface area, pore volume and average pore size are summarized in Table 1. Similar specific surface areas are obtained for (r)GO- $\text{Bi}_2\text{MoO}_6$  and bare  $\text{Bi}_2\text{MoO}_6$ , owing for the small quantity of (r)GO in the composite. A slight decrease in the specific surface area is observed when Palladium loaded on the surface. This phenomenon may be resulted from the palladium nanoparticles are blocked the slit-shaped pores. The pores volume for Pd modified rGO- $\text{Bi}_2\text{MoO}_6$  is also decreased. The decrease in specific surface area may lead to the reduction in photocatalytic activity via decrease of the adsorption capacity of pollutants in the wastewater. However, compared to the improvement of photogenerated charge carriers' separation efficiency by loading Pd on the surface, the influence of reduction in specific surface area is negligible for the overall photocatalytic activity.

### 3.5. Optical properties

The optical properties of prepared samples including pure  $\text{Bi}_2\text{MoO}_6$  and  $\text{Bi}_2\text{MoO}_6$  composites modified by GO, rGO and Pd-rGO were investigated by UV-vis DRS, and the results were depicted in Fig. 8. For the spectrum of pure  $\text{Bi}_2\text{MoO}_6$ , a steep increase in the absorbance intensity was observed when the wavelength was below 470 nm, which may have resulted from the band gap transition. The band gap energy can be calculated from the band edge with the Kubelka-Munk function as about 2.58 eV [54]. When GO

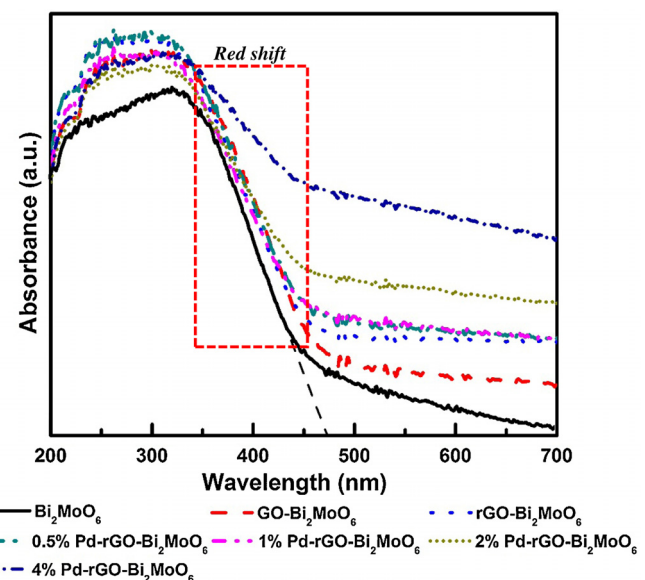


Fig. 8. UV-vis spectra for as-prepared samples.

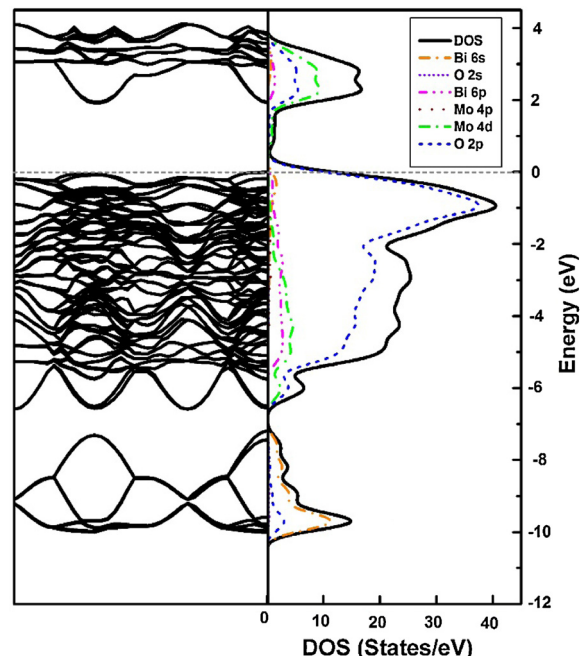


Fig. 9. Calculated band structure, and Density of states (DOS) and partial density of states (PDOS) for pure  $\text{Bi}_2\text{MoO}_6$  (Fermi level fixed at band energy of 0 eV).

combined with  $\text{Bi}_2\text{MoO}_6$ , the band gap transition was negligibly influenced; however, the visible light energy harvesting (VLEH) was improved. When GO was reduced, the VLEH capacity was further improved. The increase of absorption in the visible light region after (r)GO introduced on  $\text{Bi}_2\text{MoO}_6$  may be due to the introduction of black body properties typical of graphite-like materials [23,55]. When Pd nanoparticles were decorated on the surface of rGO- $\text{Bi}_2\text{MoO}_6$ , the VLEH capacities were significantly enhanced, improving with increasing quantities of palladium in the composites. The strong absorbance in the visible light region when Pd nanoparticles formed on the surface of composites may be due to the surface plasmon resonance (SPR) effect [56]. For pure  $\text{Bi}_2\text{MoO}_6$ , O 2p and Bi 6s states mainly contribute to the valence band, while Bi 6p, Mo 4d and O 2p states account for the conduction band (Fig. 9). The band gap value can be estimated as about 1.91 eV which is

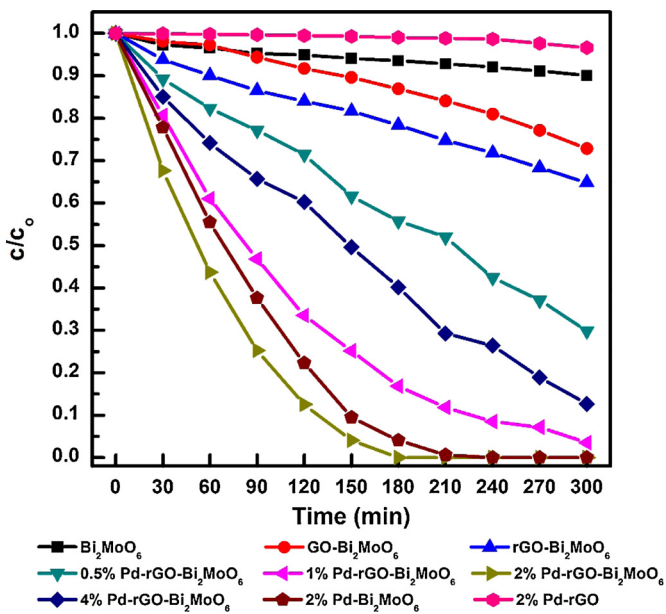


Fig. 10. Concentration profiles of phenol during the photocatalytic degradation tests in the presence different as-prepared photocatalysts under visible light irradiation.

smaller than that of the experimental result (2.58 eV) measured in Fig. 8. This phenomenon possibly resulted from the well-known limitation of GGA [57]. In conclusion, the synergetic effect of rGO and palladium Pd<sup>0</sup> nanoparticles significantly improved absorption capacity of Bi<sub>2</sub>MoO<sub>6</sub> in the visible light region of the spectrum, and lead it to become a potential candidate in visible light-driven photocatalysts.

### 3.6. Photocatalytic activity test

The photocatalytic activities of prepared photocatalysts were evaluated by degrading phenol under visible light irradiation. The relative concentration profiles of phenol as a function of irradiation time were illustrated in Fig. 10. In the presence of pure Bi<sub>2</sub>MoO<sub>6</sub>, there were about 10% of phenol photocatalytically decomposed at 300 min. For GO combined with Bi<sub>2</sub>MoO<sub>6</sub>, the photocatalytic conversion of phenol was improved from 10% to 27% at 300 min. After the reduction process of GO, the conversion was further improved to 35% at 300 min. The improvement may be caused by the electrons photogenerated by Bi<sub>2</sub>MoO<sub>6</sub> under visible light getting transferred to the GO layer, and when the oxygen groups of GO are reduced, the mobility of electrons on the graphene-like layer would be further improved. As a result, the recombination rate of photogenerated electrons and holes was significantly reduced and the photocatalytic activity of Bi<sub>2</sub>MoO<sub>6</sub> was greatly improved. Even though the Pd-rGO exhibited highly efficient degradation of organic dyes, it only lead to no more than 5% of phenol degraded over 300 min [20]. The poor activity of employing the Pd-rGO in degradation of phenol may be due to the oxidative species in the system is not strong enough to destruct the aromatic ring and no photosensitivity occurs for phenol [58]. For Pd content loaded on rGO-Bi<sub>2</sub>MoO<sub>6</sub> composites, the ternary photocatalysts performed better in the decomposition of phenol under visible light irradiation. Specifically, when the quantity of Pd increased from 0.5% to 2% in the composites, photocatalytic activity in phenol removal was greatly improved. However, when the quantity of Pd was further increased to 4%, the photocatalytic activity of the composites became worse. It might have occurred because Pd nanoparticles on the surface were also good recombination sites for photogenerated electrons and holes, resulting in the low electron/hole separation efficiency.

Table 2

Photocatalytic kinetic constants for the photocatalytic process of degradation of phenol with various photocatalysts under visible light irradiation.

Composite	k (x10 <sup>-3</sup> min <sup>-1</sup> )	R <sup>2</sup>	SE (x10 <sup>-4</sup> )	k/k <sub>Bi₂MoO₆</sub>
Bi <sub>2</sub> MoO <sub>6</sub>	0.499	0.953	0.493	1
Pd-Bi <sub>2</sub> MoO <sub>6</sub>	11.5	0.987	5.84	23.1
Pd-rGO	0.0412	0.975	0.0266	0.0826
GO-Bi <sub>2</sub> MoO <sub>6</sub>	0.657	0.978	0.437	1.32
rGO-Bi <sub>2</sub> MoO <sub>6</sub>	1.56	0.990	0.715	3.13
0.5% Pd-rGO-Bi <sub>2</sub> MoO <sub>6</sub>	2.92	0.993	1.07	5.85
1% Pd-rGO-Bi <sub>2</sub> MoO <sub>6</sub>	8.72	0.996	2.36	17.5
2% Pd-rGO-Bi <sub>2</sub> MoO <sub>6</sub>	16.1	0.990	7.13	32.3
4% Pd-rGO-Bi <sub>2</sub> MoO <sub>6</sub>	4.49	0.994	1.62	9.00

To further quantitatively compare the photocatalytic activity, the Pseudo first-order model was used to derive the photocatalytic kinetics. For low concentrations of organics in the solution (<1 × 10<sup>-4</sup> M), the model can be simplified as Eq. (4):

$$\ln\left(\frac{c_0}{c_t}\right) = k't \quad (4)$$

where  $c_0$ ,  $c_t$ ,  $k'$  and  $t$  represent initial concentration of phenol, concentration of phenol at time  $t$ , reaction rate constant and time. Simulated results of  $k'$  for each process in the presence of different photocatalysts with regard to phenol were summarized in Table 2. Based on the values for  $R^2$  and Standard Error (SE), it appears this model is highly suitable to simulate these photocatalytic processes in the presence of different as-prepared composites. Kinetics constants ( $k'$ ) may be employed to quantitatively evaluate the reaction rates for each process. It can be found that the kinetic constant increased to approximately three times when rGO combined with Bi<sub>2</sub>MoO<sub>6</sub>. It also greatly improved when Pd was loaded on rGO-Bi<sub>2</sub>MoO<sub>6</sub>. The maximum of  $k'$  was observed for the process in the presence of 2% Pd-rGO-Bi<sub>2</sub>MoO<sub>6</sub>; ~32 times higher than in the presence of pure Bi<sub>2</sub>MoO<sub>6</sub>, ~10 times higher than in the presence of rGO-Bi<sub>2</sub>MoO<sub>6</sub> and ~1.4 times higher than in the presence of 2% Pd-Bi<sub>2</sub>MoO<sub>6</sub>. This impressive enhancement in the photocatalytic degradation of phenol further confirmed the synergetic effect of palladium and rGO in these ternary composites.

### 3.7. Reusability

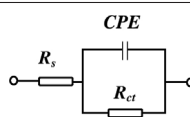
Reusability is an important parameter for evaluating a photocatalyst in terms of stability. Four runs were performed by recycling 2% Pd-rGO-Bi<sub>2</sub>MoO<sub>6</sub> for the degradation of phenol in wastewater under visible light irradiation. The concentration profiles of phenol in the solution during the degradation process were shown in Fig. 11. Complete removal of phenol can be obtained in 210 min for these four runs. A negligible difference among these four profiles can be observed, indicating the high stability of Pd-rGO-Bi<sub>2</sub>MoO<sub>6</sub> composites in the photocatalytic organic degradation process. The slight decrease in the phenol conversion may be resulted from some refractory intermediates adsorbed on the surface of the photocatalysts which reduces the reactive sites in the following run. The high reusability of Pd-rGO-Bi<sub>2</sub>MoO<sub>6</sub> composites make them an attractive candidate for use as visible light-driven photocatalysts.

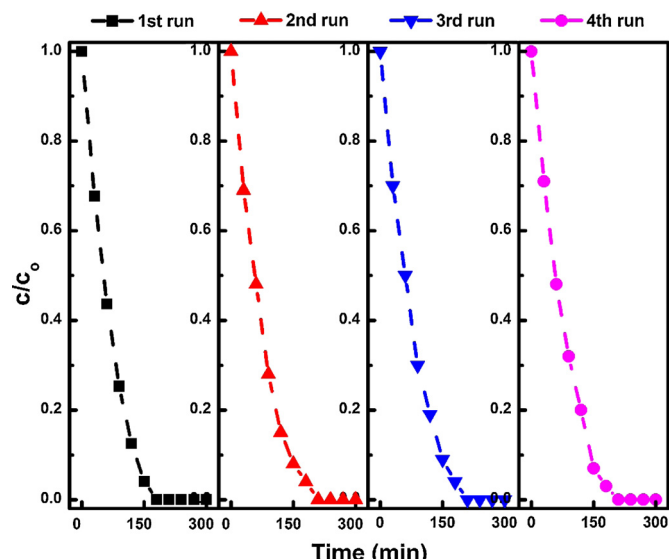
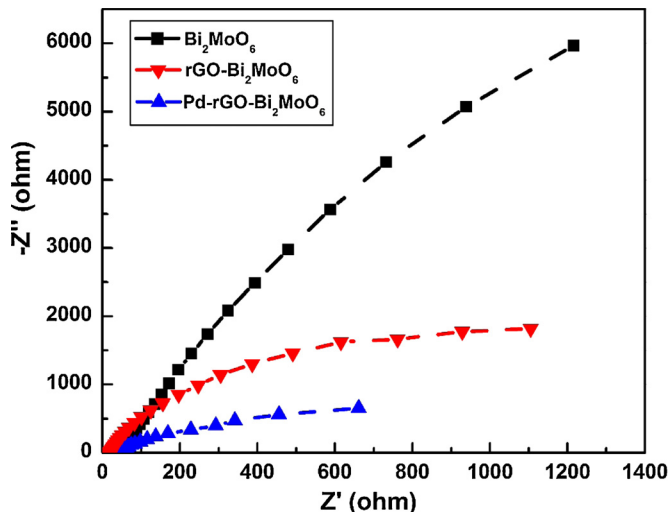
### 3.8. Mechanism exploration

To explore the enhancement mechanism in the photocatalytic activity of Pd and rGO combined with Bi<sub>2</sub>MoO<sub>6</sub>, electrochemical impedance spectroscopy (EIS) was employed to measure the separation efficiency of photogenerated electrons and holes. The EIS Nyquist plots of Bi<sub>2</sub>MoO<sub>6</sub>, rGO-Bi<sub>2</sub>MoO<sub>6</sub> and Pd-rGO-Bi<sub>2</sub>MoO<sub>6</sub> under visible light irradiation are shown in Fig. 12. Only one semicircle for each plot of all prepared samples suggest that the photocatalytic degradation process in the presence of these

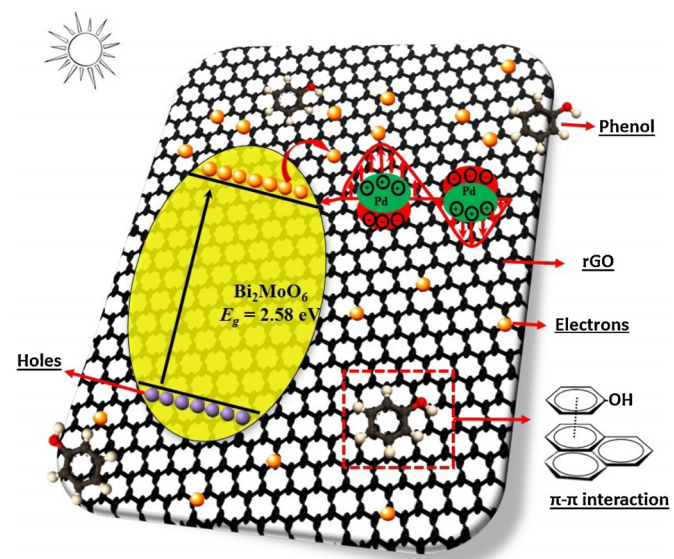
**Table 3**

Fitting results for equivalent circuits of different prepared samples.

Samples	$R_s$ ( $\Omega$ )	$R_{ct}$ ( $\Omega$ )	CPE ( $\mu\text{F}$ )	Equivalent circuits
$\text{Bi}_2\text{MoO}_6$	35.21	21630	21.52	
rGO-Bi <sub>2</sub> MoO <sub>6</sub>	40.79	3880	40.27	
Pd-rGO-Bi <sub>2</sub> MoO <sub>6</sub>	21.19	1470	45.54	

**Fig. 11.** Reusability of 2% Pd-rGO-Bi<sub>2</sub>MoO<sub>6</sub> composites with regard to phenol under visible light irradiation.**Fig. 12.** EIS Nyquist plots of the Bi<sub>2</sub>MoO<sub>6</sub>, rGO-Bi<sub>2</sub>MoO<sub>6</sub> and Pd-rGO-Bi<sub>2</sub>MoO<sub>6</sub> samples.

composites may be a simple electrode reaction and photogenerated electron transfer, and the rate may be determined by the recombination of photogenerated electron/hole pairs [59,60]. The equivalent circuits of these three processes can be simulated as shown in Table 3, where  $R_s$  is the resistance of the solution,  $R_{ct}$  represents the resistance to the electrons transfer and CPE represents the constant phase element which may be considered as a double-layered capacity. These values can be determined by the software equipped with an electrochemical analyzer (model CHI604E).  $R_{ct}$  can be calculated by the diameter of the arc in the EIS Nyquist plot; a larger arc diameter gives a higher  $R_{ct}$  value, lower electron

**Fig. 13.** Proposed mechanism of photocatalytic degradation of phenol in the presence of Pd-rGO-Bi<sub>2</sub>MoO<sub>6</sub> composites.

mobility and higher recombination of electrons and holes on the electrode. In the EIS Nyquist plot for pure Bi<sub>2</sub>MoO<sub>6</sub> with the largest diameter and highest resistance of 21,630  $\Omega$ , when rGO was coupled in the composites the diameter of the semicircle decreased and the  $R_{ct}$  value greatly reduced to 3880  $\Omega$  (~18% compared to that for pure Bi<sub>2</sub>MoO<sub>6</sub>). After Pd was further loaded on the surface of rGO-Bi<sub>2</sub>MoO<sub>6</sub>, mobility of electrons on the electrode was significantly improved with an  $R_{ct}$  value as small as 1470  $\Omega$  (~7% compared to that for pure Bi<sub>2</sub>MoO<sub>6</sub> and ~38% compared to that for rGO-Bi<sub>2</sub>MoO<sub>6</sub> composite). It suggests that the electrons/holes separation efficiency was greatly improved when rGO and Pd were loaded on Bi<sub>2</sub>MoO<sub>6</sub>, which directly resulted in the enhanced visible light-driven photocatalytic activity.

The proposed mechanism was summarized in Fig. 13 on the basis of results obtained and discussed above. Specifically, when rGO combined with Bi<sub>2</sub>MoO<sub>6</sub>, the rGO layer may perform as an electron acceptor, which means photogenerated electrons on the conduction band of Bi<sub>2</sub>MoO<sub>6</sub> may transfer to the rGO layer so as to suppress their recombination with holes on the valence band of Bi<sub>2</sub>MoO<sub>6</sub> [12,27,61]. When Pd content was loaded on the surface of rGO-Bi<sub>2</sub>MoO<sub>6</sub> composites, Pd nanoparticles distributed on both rGO and Bi<sub>2</sub>MoO<sub>6</sub> may have absorbed visible light energy to produce electrons due to the SPR effect (the SPR peaks of Pd nanostructure can be tuned from 410 nm to 870 nm [18,19]). Furthermore, Cl<sup>-</sup> was also found in the composites (Fig. 3e). The anion may be oxidized to Cl<sup>0</sup>, which is itself a strong oxidizing agent that may be capable of oxidizing phenol to return to its reduced, anionic state (Cl<sup>-</sup>) [62]. In addition, because of the strong  $\pi$ - $\pi$  interaction between aromatic rings of phenol and rGO, phenol may also be much easier to adsorb onto the surface of rGO-Bi<sub>2</sub>MoO<sub>6</sub> composite compared to pure Bi<sub>2</sub>MoO<sub>6</sub> [63]. In conclusion, the improved separation efficiency of photogenerated electron-hole pairs via capture of palladium nanoparticles, transportation through the

rGO, increased harvesting intensity of visible light photons due to the SPR effect and a narrowed band gap, and strong adsorption of phenol on rGO layers contributed to an enhanced photocatalytic activity towards the degradation of phenol under visible light irradiation.

#### 4. Conclusions

A ternary Pd-rGO-Bi<sub>2</sub>MoO<sub>6</sub> photocatalyst composite was first prepared via solvothermal-photo reduction method. It was found to provide enhanced visible light-driven photocatalytic activity in the removal of phenol in wastewater. The enhanced performance may be attributed to the high separation efficiency of photogenerated electrons and holes. Electrons may be transferred to either the rGO layer or the palladium nanoparticles on the surface. In addition, palladium nanoparticles on the surface can also produce electrons due to the SPR effect. This synergistic effect lead to the excellent visible light-driven photocatalytic degradation of phenol in the wastewater. At last, we believe this work will provide a new idea for the rGO based ternary composites in the area of visible light-driven photocatalysis and shed light on the significances of applying palladium nanoparticles to improve the visible light-induced photocatalytic activity.

#### Acknowledgements

Financial support for this work was provided by the Natural Sciences and Engineering Research Council of Canada. Xiangchao Meng was the recipient of a scholarship from the China Scholarship Council for the duration of this work.

#### References

- [1] D.F. Ollis, H. Al-Ekabi, TiO<sub>2</sub> photocatalytic purification and treatment of water and air, in: Photocatalytic Purification and Treatment of Water and Air: Proceedings of the 1st International Conference, Elsevier Science Ltd., 1993.
- [2] A. Kudo, Recent progress in the development of visible light-driven powdered photocatalysts for water splitting, *Int. J. Hydrogen Energy* 32 (2007) 2673–2678.
- [3] Y. Wang, Q. Wang, X. Zhan, F. Wang, M. Safdar, J. He, Visible light driven type II heterostructures and their enhanced photocatalysis properties: a review, *Nanoscale* 5 (2013) 8326–8339.
- [4] X. Meng, Z. Zhang, Bismuth-based photocatalytic semiconductors: introduction, challenges and possible approaches, *J. Mol. Catal. A: Chem.* 423 (2016) 533–549.
- [5] X. Meng, Z. Zhang, Facile synthesis of BiOBr/Bi<sub>2</sub>WO<sub>6</sub> heterojunction semiconductors with high visible-light-driven photocatalytic activity, *J. Photochem. Photobiol. A: Chem.* 310 (2015) 33–44.
- [6] M. Ni, M.K. Leung, D.Y. Leung, K. Sumathy, A review and recent developments in photocatalytic water-splitting using TiO<sub>2</sub> for hydrogen production, *Renew. Sustain. Energy Rev.* 11 (2007) 401–425.
- [7] Y. Shi, S. Feng, C. Cao, Hydrothermal synthesis and characterization of Bi<sub>2</sub>MoO<sub>6</sub> and Bi<sub>2</sub>WO<sub>6</sub>, *Mater. Lett.* 44 (2000) 215–218.
- [8] L. Zhang, T. Xu, X. Zhao, Y. Zhu, Controllable synthesis of Bi<sub>2</sub>MoO<sub>6</sub> and effect of morphology and variation in local structure on photocatalytic activities, *Appl. Catal. B: Environ.* 98 (2010) 138–146.
- [9] X. Zhao, J. Qu, H. Liu, Z. Qiang, R. Liu, C. Hu, Photoelectrochemical degradation of anti-inflammatory pharmaceuticals at Bi<sub>2</sub>MoO<sub>6</sub>-boron-doped diamond hybrid electrode under visible light irradiation, *Appl. Catal. B: Environ.* 91 (2009) 539–545.
- [10] B. Yuan, C. Wang, Y. Qi, X. Song, K. Mu, P. Guo, L. Meng, H. Xi, Decorating hierarchical Bi<sub>2</sub>MoO<sub>6</sub> microspheres with uniformly dispersed ultrafine Ag nanoparticles by an in situ reduction process for enhanced visible light-induced photocatalysis, *Colloids Surf. A* 425 (2013) 99–107.
- [11] S. Wang, X. Yang, X. Zhang, X. Ding, Z. Yang, K. Dai, H. Chen, A plate-on-plate sandwiched Z-scheme heterojunction photocatalyst: BiOBr-Bi<sub>2</sub>MoO<sub>6</sub> with enhanced photocatalytic performance, *Appl. Surf. Sci.* (2016).
- [12] P. Wang, Y. Ao, C. Wang, J. Hou, J. Qian, A one-pot method for the preparation of graphene-Bi<sub>2</sub>MoO<sub>6</sub> hybrid photocatalysts that are responsive to visible-light and have excellent photocatalytic activity in the degradation of organic pollutants, *Carbon* 50 (2012) 5256–5264.
- [13] G. Tian, Y. Chen, J. Zhou, C. Tian, R. Li, C. Wang, H. Fu, In situ growth of Bi<sub>2</sub>MoO<sub>6</sub> on reduced graphene oxide nanosheets for improved visible-light photocatalytic activity, *CrystEngComm* 16 (2014) 842–849.
- [14] Y. Zhang, Y. Zhu, J. Yu, D. Yang, T.W. Ng, P.K. Wong, J.C. Yu, Enhanced photocatalytic water disinfection properties of Bi<sub>2</sub>MoO<sub>6</sub>-RGO nanocomposites under visible light irradiation, *Nanoscale* 5 (2013) 6307–6310.
- [15] Y. Hao, X. Dong, X. Wang, S. Zhai, H. Ma, X. Zhang, Controllable electrostatic self-assembly of sub-3 nm graphene quantum dots incorporated into mesoporous Bi<sub>2</sub>MoO<sub>6</sub> frameworks: efficient physical and chemical simultaneous co-catalysis for photocatalytic oxidation, *J. Mater. Chem. A* 4 (2016) 8298–8307.
- [16] Q. Xiang, J. Yu, M. Jaroniec, Graphene-based semiconductor photocatalysts, *Chem. Soc. Rev.* 41 (2012) 782–796.
- [17] J. Zhang, C. Niu, J. Ke, L. Zhou, G. Zeng, Ag/AgCl/Bi<sub>2</sub>MoO<sub>6</sub> composite nanosheets: a plasmonic Z-scheme visible light photocatalyst, *Catal. Commun.* 59 (2015) 30–34.
- [18] Y. Xiong, B. Wiley, J. Chen, Z.-Y. Li, Y. Yin, Y. Xia, Corrosion-based synthesis of single-crystal Pd nanoboxes and nanocages and their surface plasmon properties, *Angew. Chem. Int. Ed.* 44 (2005) 7913–7917.
- [19] Y. Xiong, J. Chen, B. Wiley, Y. Xia, Y. Yin, Z.-Y. Li, Size-dependence of surface plasmon resonance and oxidation for Pd nanocubes synthesized via a seed etching process, *Nano Lett.* 5 (2005) 1237–1242.
- [20] S. Li, H. Li, J. Liu, H. Zhang, Y. Yang, Z. Yang, L. Wang, B. Wang, Highly efficient degradation of organic dyes by palladium nanoparticles decorated on 2D magnetic reduced graphene oxide nanosheets, *Dalton Trans.* 44 (2015) 9193–9199.
- [21] J. Liu, X. Huo, T. Li, Z. Yang, P. Xi, Z. Wang, B. Wang, Palladium nanoparticles bonded to two-dimensional iron oxide graphene nanosheets: a synergistic and highly reusable catalyst for the Tsuji–Trost reaction in water and air, *Chem. Eur. J.* 20 (2014) 11549–11555.
- [22] X. Meng, Z. Zhang, Pd-doped Bi<sub>2</sub>MoO<sub>6</sub> plasmonic photocatalysts with enhanced visible light photocatalytic performance, *Appl. Surf. Sci.* 392 (2016) 169–180.
- [23] S. Gupta, V. Subramanian, Encapsulating Bi<sub>2</sub>Ti<sub>2</sub>O<sub>7</sub> (BTO) with reduced graphene oxide (RGO): an effective strategy to enhance photocatalytic and photoelectrocatalytic activity of BTO, *ACS Appl. Mater. Interfaces* 6 (2014) 18597–18608.
- [24] B. Allured, S. DelaCruz, T. Darling, M.N. Huda, V. Subramanian, Enhancing the visible light absorbance of Bi<sub>2</sub>Ti<sub>2</sub>O<sub>7</sub> through Fe-substitution and its effects on photocatalytic hydrogen evolution, *Appl. Catal. B: Environ.* 144 (2014) 261–268.
- [25] W.F. Yao, H. Wang, X.H. Xu, X.N. Yang, Y. Zhang, S.X. Shang, M. Wang, Preparation and photocatalytic property of La (Fe)-doped bismuth titanate, *Appl. Catal. A: Gen.* 251 (2003) 235–239.
- [26] R. Liu, P. Wang, X. Wang, H. Yu, J. Yu, UV- and visible-light photocatalytic activity of simultaneously deposited and doped Ag/Ag(I)-TiO<sub>2</sub> photocatalyst, *J. Phys. Chem. C* 116 (2012) 17721–17728.
- [27] J. Bi, W. Fang, L. Li, X. Li, M. Liu, S. Liang, Z. Zhang, Y. He, H. Lin, L. Wu, S. Liu, P.K. Wong, Ternary reduced-graphene-oxide/Bi<sub>2</sub>MoO<sub>6</sub>/Au nanocomposites with enhanced photocatalytic activity under visible light, *J. Alloys Compd.* 649 (2015) 28–34.
- [28] X. Meng, Z. Zhang, Plasmonic ternary Ag-rGO-Bi<sub>2</sub>MoO<sub>6</sub> composites with enhanced visible light-driven photocatalytic activity, *J. Catal.* 344 (2016) 616–630.
- [29] G. Fu, L. Tao, M. Zhang, Y. Chen, Y. Tang, J. Lin, T. Lu, One-pot, water-based and high-yield synthesis of tetrahedral palladium nanocrystal decorated graphene, *Nanoscale* 5 (2013) 8007–8014.
- [30] I. Oller, S. Malato, J.A. Sánchez-Pérez, Combination of Advanced Oxidation Processes and biological treatments for wastewater decontamination—a review, *Sci. Total Environ.* 409 (2011) 4141–4166.
- [31] P.R. Gogate, Treatment of wastewater streams containing phenolic compounds using hybrid techniques based on cavitation: a review of the current status and the way forward, *Ultrason. Sonochem.* 15 (2008) 1–15.
- [32] Y. Liu, Y. Zhang, G. Ma, Z. Wang, K. Liu, H. Liu, Ethylene glycol reduced graphene oxide/polypyrrole composite for supercapacitor, *Electrochim. Acta* 88 (2013) 519–525.
- [33] W. Kohn, L.J. Sham, Self-consistent equations including exchange and correlation effects, *Phys. Rev.* 140 (1965) A1133.
- [34] G. Paolo, B. Stefano, B. Nicola, C. Matteo, C. Roberto, C. Carlo, C. Davide, L.C. Guido, C. Matteo, D. Ismaila, C. Andrea Dal, G. Stefano de, F. Stefano, F. Guido, G. Ralph, G. Uwe, G. Christos, K. Anton, L. Michele, M.-S. Layla, M. Nicola, M. Francesco, M. Riccardo, P. Stefano, P. Alfredo, P. Lorenzo, S. Carlo, S. Sandro, S. Gabriele, P.S. Ari, S. Alexander, U. Paolo, M.W. Renata, QUANTUM ESPRESSO: a modular and open-source software project for quantum simulations of materials, *J. Phys.: Condens. Matter* 21 (2009) 395502.
- [35] F. Pertlik, J. Zemann, Neubestimmung der kristallstruktur des Köchlinit, *Fortschr. Miner.* Beih. 60 (1982) 162–163.
- [36] C. Bichler, M. Bischoff, H. Langowski, U. Moosheimer, 39th Annual Technical Conference of the Society of Vacuum Coaters, Philadelphia, USA, May, 5, 1996.
- [37] P. Zeng, Q. Zhang, T. Peng, X. Zhang, One-pot synthesis of reduced graphene oxide-cadmium sulfide nanocomposite and its photocatalytic hydrogen production, *Phys. Chem. Chem. Phys.* 13 (2011) 21496–21502.
- [38] Y.-S. Xu, W.-D. Zhang, Monodispersed Ag<sub>3</sub>PO<sub>4</sub> nanocrystals loaded on the surface of spherical Bi<sub>2</sub>MoO<sub>6</sub> with enhanced photocatalytic performance, *Dalton Trans.* 42 (2013) 1094–1101.
- [39] C. Wagner, G. Muilenberg, *Handbook of X-ray Photoelectron Spectroscopy*, Perkin-Elmer, 1979.
- [40] J.H. Scofield, Hartree-Slater subshell photoionization cross-sections at 1254 and 1487 eV, *J. Electron. Spectrosc.* 8 (1976) 129–137.

[41] D.R. Penn, Quantitative chemical analysis by ESCA, *J. Electron. Spectrosc.* 9 (1976) 29–40.

[42] M.A. Butler, D.S. Ginley, Prediction of flatband potentials at Semiconductor-electrolyte interfaces from atomic electronegativities, *J. Electrochim. Soc.* 125 (1978) 228–232.

[43] A.H. Nethercot, Prediction of fermi energies and photoelectric thresholds based on electronegativity concepts, *Phys. Rev. Lett.* 33 (1974) 1088–1091.

[44] R.D. Seals, R. Alexander, L.T. Taylor, J.G. Dillard, Core electron binding energy study of group IIb-VIIa compounds, *Inorg. Chem.* 12 (1973) 2485–2487.

[45] S.R.G. Carrazán, C. Martín, V. Rives, R. Vidal, An FT-IR spectroscopy study of the adsorption and oxidation of propene on multiphase Bi, Mo and Co catalysts, *Spectrochim. Acta Part A* 52 (1996) 1107–1118.

[46] F. Trifirò, H. Hoser, R.D. Scarle, Relationship between structure and activity of mixed oxides as oxidation catalysts: I. Preparation and solid state reactions of Bi-molybdates, *J. Catal.* 25 (1972) 12–24.

[47] P. Wang, J. Wang, X. Wang, H. Yu, J. Yu, M. Lei, Y. Wang, One-step synthesis of easy-recycling TiO<sub>2</sub>-rGO nanocomposite photocatalysts with enhanced photocatalytic activity, *Appl. Catal. B: Environ.* 132–133 (2013) 452–459.

[48] H. Adamu, P. Dubey, J.A. Anderson, Probing the role of thermally reduced graphene oxide in enhancing performance of TiO<sub>2</sub> in photocatalytic phenol removal from aqueous environments, *Chem. Eng. J.* 284 (2016) 380–388.

[49] P.W. Voorhees, The theory of Ostwald ripening, *J. Stat. Phys.* 38 (1985) 231–252.

[50] H.G. Yang, H.C. Zeng, Preparation of hollow anatase TiO<sub>2</sub> nanospheres via ostwald ripening, *J. Phys. Chem. B* 108 (2004) 3492–3495.

[51] K. Sing, D. Everett, R. Haul, L. Moscou, R. Pierotti, J. Rouquerol, T. Siemieniewska, Physical and biophysical chemistry division commission on colloid and surface chemistry including catalysis, *Pure Appl. Chem.* 57 (1985) 603–619.

[52] M. Kruk, M. Jaroniec, Gas adsorption characterization of ordered organic-inorganic nanocomposite materials, *Chem. Mater.* 13 (2001) 3169–3183.

[53] M. Thommes, K. Kaneko, V. Neimark Alexander, P. Olivier James, F. Rodriguez-Reinoso, J. Rouquerol, S.W. Sing Kenneth, Physisorption of gases, with special reference to the evaluation of surface area and pore size distribution (IUPAC Technical Report), *Pure Appl. Chem.* (2015) 1051.

[54] G. Liao, S. Chen, X. Quan, H. Yu, H. Zhao, Graphene oxide modified g-C<sub>3</sub>N<sub>4</sub> hybrid with enhanced photocatalytic capability under visible light irradiation, *J. Mater. Chem.* 22 (2012) 2721–2726.

[55] E. Gao, W. Wang, M. Shang, J. Xu, Synthesis and enhanced photocatalytic performance of graphene-Bi<sub>2</sub>WO<sub>6</sub> composite, *Phys. Chem. Chem. Phys.* 13 (2011) 2887–2893.

[56] S. Linic, P. Christopher, D.B. Ingram, Plasmonic-metal nanostructures for efficient conversion of solar to chemical energy, *Nat. Mater.* 10 (2011) 911–921.

[57] K. Lai, W. Wei, Y. Dai, R. Zhang, B. Huang, DFT calculations on structural and electronic properties of Bi<sub>2</sub>MO<sub>6</sub> (M = Cr, Mo W), *Rare Met.* 30 (2011) 166–172.

[58] M. Vautier, C. Guillard, J.-M. Herrmann, Photocatalytic degradation of dyes in water: case study of indigo and of indigo carmine, *J. Catal.* 201 (2001) 46–59.

[59] J.M. Kesselman, G.A. Shreve, M.R. Hoffmann, N.S. Lewis, Flux-Matching conditions at TiO<sub>2</sub> photoelectrodes: is interfacial electron transfer to O<sub>2</sub> rate-Limiting in the TiO<sub>2</sub>-Catalyzed photochemical degradation of organics? *J. Phys. Chem.* 98 (1994) 13385–13395.

[60] B. Xin, Z. Ren, H. Hu, X. Zhang, C. Dong, K. Shi, L. Jing, H. Fu, Photocatalytic activity and interfacial carrier transfer of Ag-TiO<sub>2</sub> nanoparticle films, *Appl. Surf. Sci.* 252 (2005) 2050–2055.

[61] H. Zhang, X. Lv, Y. Li, Y. Wang, J. Li, P25-Graphene composite as a high performance photocatalyst, *Acs Nano* 4 (2010) 380–386.

[62] J. Gamage McEvoy, W. Cui, Z. Zhang, Synthesis and characterization of Ag/AgCl-activated carbon composites for enhanced visible light photocatalysis, *Appl. Catal. B: Environ.* 144 (2014) 702–712.

[63] Y. Wen, H. Ding, Y. Shan, Preparation and visible light photocatalytic activity of Ag/TiO<sub>2</sub>/graphene nanocomposite, *Nanoscale* 3 (2011) 4411–4417.